
Scaling of Hybrid QDs-Graphene Photodetectors to Subwavelength Dimension

Gökhan Kara^a, Patrik Rohner^{a,b}, Erfu Wu^a, Dmitry N. Dirin^{b,d}, Roman Furrer^a, Dimos Poulikakos^c, Maksym V. Kovalenko^{b,d}, Michel Calame^{a,e}, Ivan Shorubalko^{a,*}

(a) Laboratory for Transport at Nanoscale Interfaces, Empa – Swiss Federal Laboratories for Materials Science and Technology, CH-8600 Dübendorf, Switzerland

(b) Department of Chemistry and Applied Biosciences, ETH – Swiss Federal Institute of Technology Zurich, CH-8093 Zurich, Switzerland

(c) Laboratory of Thermodynamics in Emerging Technologies, Department of Mechanical and Process Engineering, ETH – Swiss Federal Institute of Technology Zurich, CH-8092 Zurich, Switzerland

(d) Laboratory for Thin Films and Photovoltaics, Empa – Swiss Federal Laboratories for Materials Science and Technology, CH-8600 Dübendorf, Switzerland

(e) Department of Physics and Swiss Nanoscience Institute, University of Basel, CH-4056 Basel, Switzerland

* Email: ivan.shorubalko@empa.ch

Abstract

Emerging colloidal quantum dot (cQD) photodetectors currently challenge established state-of-the-art infrared photodetectors in response speed, spectral tunability, simplicity of solution processable fabrication, and integration onto curved or flexible substrates. Hybrid phototransistors based on 2D materials and cQDs, in particular, are promising due to their inherent photogain enabling direct photosignal enhancement. The photogain is sensitive to both, measurement conditions and photodetector geometry. This makes the cross-comparison of devices reported in the literature rather involved. Here, the effect of device length L and width W scaling to sub-wavelength dimensions (sizes down to 500 nm) on the photoresponse of graphene-PbS cQD phototransistors was experimentally investigated. Photogain and responsivity were found to scale with $1/LW$, whereas the photocurrent and specific detectivity were independent of geometrical parameters. The measurements were performed at scaled bias voltage conditions for comparable currents. Contact effects were found to limit the photoresponse for devices with $L < 3 \mu\text{m}$. The relation of gate voltage, bias current, light intensity, and frequency on the photoresponse was investigated in detail, and a photogating efficiency to assess the cQD-graphene interface is presented. In particular, the specific detectivity values in the range between 10^8 to 10^9 Jones (wavelength of 1550 nm, frequency 6 Hz, room temperature) were found to be limited by the charge transfer across the photoactive interface.

Keywords: colloidal quantum dots, graphene, phototransistors, infrared photodetectors, scaling, subwavelength

Introduction

Emerging photodetectors based on colloidal quantum dots (cQDs) are currently challenging state-of-the-art infrared (IR) photodetectors by low cost solution processing^{1,2}, simple spectral tunability^{1,2}, multiband absorption³⁻⁵, response speed⁶⁻⁸, and integration onto flexible substrates⁹⁻¹². PbS cQDs SWIR photodiode arrays were recently fabricated with a pixel pitch of 1.62 μm .¹³ This is about five times smaller than the pixel size of common InGaAs photodetectors. Reduced dimension are, on the contrary, also limiting the number of photons reaching a detector. The integration of photonic structures is, thus, an attractive way to enhance light-matter interaction in cQD photodetectors.^{14,15} Another way to overcome low light levels is by coupling a light absorber with a transistor. By introducing PbS cQDs as a photogate to a graphene field effect transistor (GFET), photoresponsivities of 10^6 to 10^7 A/W were demonstrated.^{16,17} The high responsivity values were also reflected in the specific detectivity of 10^{13} Jones at room temperature¹⁶ that is comparable to commercial InGaAs photodetectors.

Research in hybrid phototransistors is focused on reducing dark currents by exchanging the transistor channel material with TMDCs¹⁸⁻²¹ or metal oxides^{12,22}, energy barrier engineering^{9,19,23,24}, longer charge extraction distance in the cQD films²⁵, extending the spectral range to longer wavelength^{21,26,27}, or technological applicability to flexible substrates^{9,11,12} and printing^{26,28,29}. Although it is commonly reported that the photogain G_{ph} follows a $1/L^2$ dependence in those devices³⁰⁻³², limited effort has been spent to experimentally validate this prediction. In addition, the photoresponse is highly dependent on measurement conditions (e.g., bias, illumination), geometry, and batch-specific fabrication. Thus, reproducibility and the cross-comparison of individual reports remain highly involved, and derived scaling laws are inconclusive.

Here, we experimentally demonstrate the scaling of hybrid graphene - PbS cQD phototransistors with channel length, width, and cQD film thickness. We highlight a $1/LW$ dependence of the photogain and responsivity, and a dimension-independent photocurrent and specific detectivity at scaled bias voltage condition for comparable currents. We further show the photoresponse's gate voltage, bias current, light intensity, and frequency dependency and derive a photogating efficiency for a cQD-graphene interface evaluation.

Results and Discussion

Photocurrent Relation of Hybrid Phototransistors

Figure 1 (a) shows a cross-section of a hybrid phototransistor. Two gold electrodes (source and drain) contact the graphene channel, and a p-Si back gate enables charge carrier density tuning in the channel by the field effect. The phototransistor has a channel length (L), width (W), and a cQDs film thickness t_{QDs} as the photogate on top. The incoming light creates electron-hole (e-h) pairs in the absorbing cQD layer. The Fermi level alignment between

graphene and the cQD film causes an electric field at the interface (depletion region) that separates the photo-generated e-h pairs and leads to the commonly observed hole transfer to the graphene channel. The electrons stay trapped in the film for a time τ_{trap} , gating the channel.¹⁶ The photoinitiated e-h separation current between the cQDs film and graphene is small compared to the channel current I_{DS} and is thus neglected. The photogate modulation of I_{DS} is an enhancement of the photosignal and is described as photogain by the rate equation

$$G_{ph} = \frac{\# \text{ charges observed}}{\# \text{ photogenerated charges}} = \frac{1/\tau_{transit}}{1/\tau_{trap}}. \quad (1)$$

$\tau_{transit}$ is the transit time of a charge carrier in the channel between source and drain contacts.^{30,32,33} Within the Drude model, the transit time can be stated by bias condition and geometry of the channel and leads to

$$G_{ph} = \frac{1}{L^2} \tau_{trap} \mu V_{DS}. \quad (2)$$

V_{DS} is the bias voltage between source and drain, and μ the charge carrier mobility in the channel. The photocurrent of the hybrid phototransistors can thus be described by

$$I_{ph} = G_{ph} \phi \eta_{Gph} e, \quad (3)$$

where e the elementary charge, and η_{Gph} is a photogating efficiency describing how likely an incoming photon is creating a charge photogating the transistor channel.^{30,34} The photonflux $\phi = P_{in}/E_{ph}$ is defined by the incoming light power P_{in} and photon energy $E_{ph} = hc/\lambda$. h is Planck's constant, c the speed of light, and λ the wavelength of the incoming light. Thus, the photoresponsivity

$$R = \frac{I_{ph}}{P_{in}}, \quad (4)$$

is proportional to the G_{ph} and often stated as $R \sim 1/L^2$.

Figure 1 (a) also shows the experimental setup used to characterize the photoresponse of the investigated detectors. A bias voltage V_{DS} was applied between the source and drain contacts, and the current I_{DS} was measured simultaneously. A gate voltage V_G was applied to the back gate to control the 2D charge carrier density $n = C_{SiO_2} V_G / e$ in the graphene channel, where $C_{SiO_2} \approx 11.9 \text{ nF/cm}^2$ is the capacitance of the gate oxide. The incoming light was chopped at a frequency f_{chop} . This light modulation induced an AC photocurrent on top of I_{DS} that was extracted as a voltage drop V_{ph} over a shunt resistance. The incoming light power was characterized by a reference detector. The calculated the photoresponsivity for a sub-wavelength dimensioned device of $0.5 \times 0.5 \text{ }\mu\text{m}^2$ is shown in Figure 1 (b). The inset shows the AFM image of the characterized device before cQD sensitization. A photoresponsivity of 150 A/W was reached at the first excitonic peak at 1530 nm . The spin-coating of the PbS cQDs lead to a blue shift of about 70 nm compared to their excitonic peak at 1600 nm

(diameter ~ 6 nm)³⁵ after synthesis. All measurements were performed in vacuum and at room temperature.

Further, electrohydrodynamic nanoprinting (EHD) and layer-by-layer (LbL) spin coating were compared to assess the influence of cQD deposition techniques on the photoresponse. First, in Figure 1 (c), the deposition of cQDs by EHD printing is depicted. By applying an AC voltage between the gold coated nozzle and the substrate, cQDs accumulate at the formed meniscus, and droplets markedly smaller than the nozzle diameter are pulled out by the electric field from the apex of the meniscus. This enables printing features with a resolution in the 100 nm range.^{36,37} For PbS cQDs in particular, a resolution of ~ 1 μm was previously demonstrated.²⁸ This method enables precise spatial control of placing cQDs in a desired geometrical pattern. After printing, a solid-state ligand exchange treatment was performed to substitute the native oleic acid with ethane-1,2-dithiol ligands. This single-step treatment reduces the interparticle distance, a t_{QDs} shrinkage of about 40% was observed, leading to conductive films. Additionally, the extra control of film thickness by EHD printing on a single sample level allowed to vary t_{QDs} between 65 to 120 nm. The geometry of the device channels were $L \times W = 20 \times 5$ μm^2 .

The second applied method was the layer-by-layer (LbL) spin coating. A thin layer of cQDs was spin coated and directly treated with a solid-state ligand exchange procedure to EDT. These two steps were repeated six times, resulting in t_{QDs} of 170 nm. By this method, devices with different L ranging from 20 down to 0.5 μm and a $W = 5$ μm were sensitized with cQDs. In addition, the W scaling was investigated by changing the width between 5 down to 0.5 μm with a fixed $L = 20$ μm . Figure 1 (d) shows the investigated devices with the LbL spin-coating approach before deposition. In contrast to printing, the entire sample was covered with one cQD thickness (inset). The LbL spin coating has been proven to yield dense and crack-free conductive films³⁸, optimally suited for solar cells and photodetectors.³⁹⁻⁴¹

Figure 2 (a) shows the characterized devices of EHD-printed cQDs films with different layer thicknesses. From top to down, the plots show the source-drain currents I_{DS} , transconductance $g_m = dI_{DS}/dV_G$ and the amplitude of the photocurrent $|I_{ph}|$ while the gate voltage V_G was swept. g_m was derived by a numerical derivative from I_{DS} . The measurements were performed at a bias voltage V_{DS} of 100 mV, irradiance \mathbb{I}_{in} of 120 $\mu\text{W}/\text{cm}^2$, chopping frequency f_{chop} of 6 Hz, and the curves were corrected by the individual Dirac point voltage V_D (charge neutrality point) of the GFETs (average V_D of -20 V). The first excitonic peak of the cQDs shifted to a wavelength λ of 1345 nm (shift of about 250 nm). The blue shift of the absorption peak might be explained by oxidation of the cQDs during printing. The maximum of the measured photocurrent I_{ph} was found at the left, hole-doped region p , and right, electron-doped region n , of the Dirac point. The dashed lines (red and blue) indicate where the maximum photocurrents were measured that, on average, corresponds to 10 V ($n \approx 7 \times 10^{11}$ $1/\text{cm}^2$) from the Dirac point.

The solid red and blue lines (p- and n-doped region) in the g_m and I_{DS} plots indicate

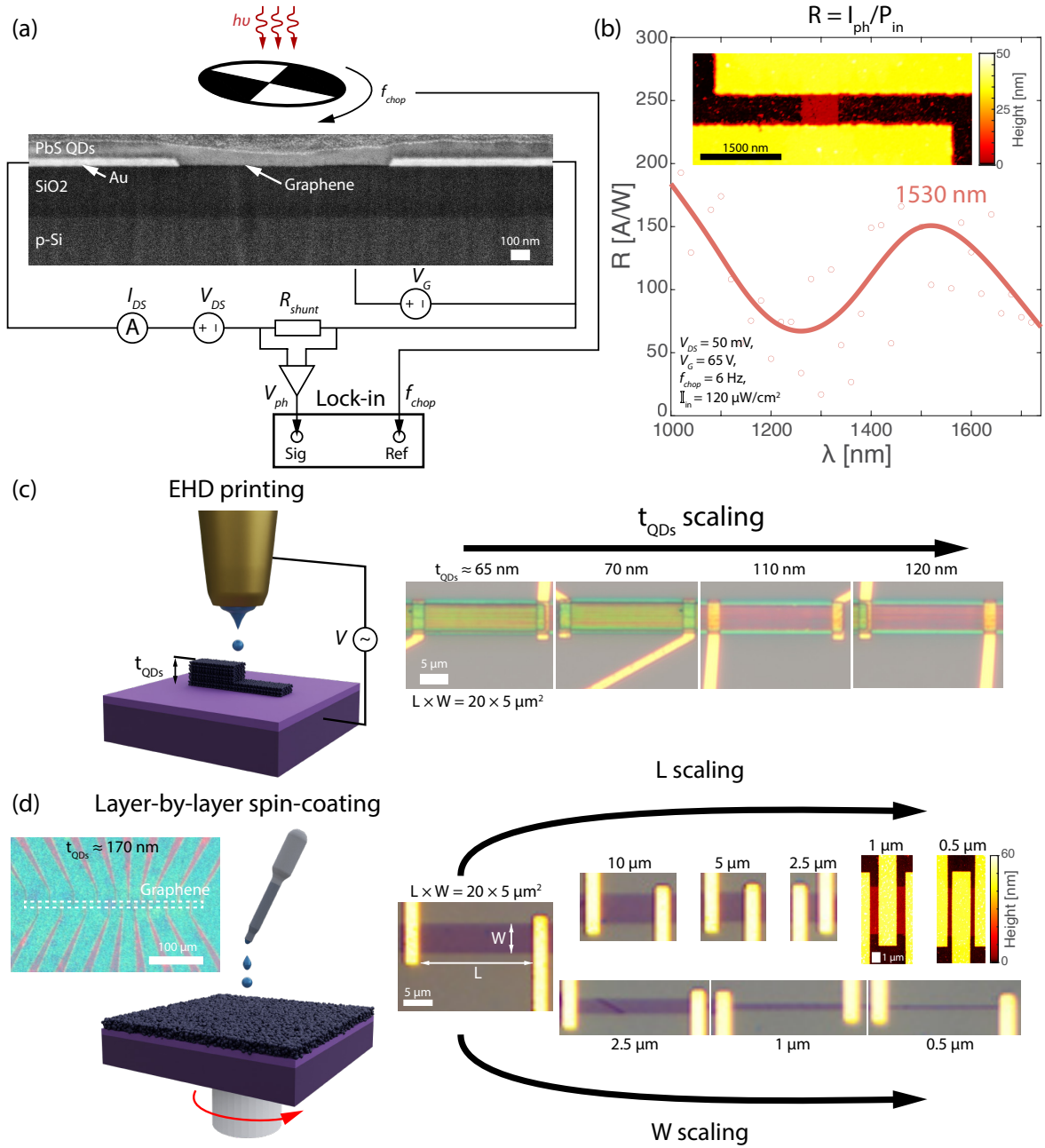


Figure 1: Photodetector characterization scheme and used PbS cQD deposition techniques. (a) the cross-section of a hybrid graphene-PbS cQD phototransistor. Two Au electrodes contacted the graphene channel, and 285 nm SiO₂ separated the p-Si back gate from the channel. A V_{DS} bias was applied, and V_G on the back gate modulated the 2D charge carrier density n in the channel. The incoming light with energy $E_{ph} = hc/\lambda$ was chopped at a frequency f_{chop} . Photocurrents were extracted with a lock-in amplifier measuring V_{ph} over a shunt resistance. (b) Photoresponsivity R of a subwavelength dimensioned photodetector of $0.5 \times 0.5 \mu\text{m}^2$. The inset shows the AFM image of the GFET before cQD deposition. (c) EHD printing illustration and photodetectors with a channel geometry $L \times W$ of $20 \times 5 \mu\text{m}^2$. The PbS cQD thickness was varied. (d) LbL spin coating illustration. The inset on the left shows an optical microscope image after PbS cQD fabrication. The L- and W-scaling devices are shown before cQD deposition (optical microscope and AFM).

where g_m reaches about a constant maximum, as illustrated for the device with $t_{QDs} = 120$

nm. The maxima of the photocurrent coincide with this region and thus are found where the transconductance is the highest, as reported previously.⁴² The yellow shaded region of Figure 2 (a) indicates the influenced region by random potential fluctuations around the Dirac point in graphene. In this region, the applied gate voltage loses its ability to tune n up to a point where charges are only redistributed locally (e-h charge puddles) and, thus, does not affect the conductivity anymore. This causes a drop of g_m towards the Dirac point and depends on residual doping and temperature $n^* + n^{th}$.⁴³

Figure 2 (b) depicts the four devices' AFM images after ligand exchange treatment. Thicker cQD films absorb more light reaching 100% absorption at about 500 nm for an absorption coefficient of $\sim 1 \times 10^5$ cm.³⁵ Correspondingly, an increasing trend of the photocurrent with thicker t_{QDs} films is observed in the bottom panel of Figure 2 (a). However, to extract charges from the cQD layer, they need to be in the depletion region close to the interface.²⁵ This is why a saturation of the photocurrent is expected before $t_{QDs} \approx 500$ nm is reached. In a previous study, this saturation thickness was found to be about 160 nm for EHD-printed cQD films.²⁸

The photoresponsivity R is used to assess detectors' efficiency in converting light into a photocurrent. However, R is a derived quantity and describes the proportionality between the photocurrent and the incoming light power.³⁴ Thus, in this study, the main focus was put on I_{ph} as the measured quantity at comparable conditions across the investigated devices. Also, applying a constant bias voltage might not always be applicable over the different length scales as the current is proportionally increasing with $1/L$. A comparison should thus aim to keep the applied electric field $|\vec{E}| = V_{DS}/L$ constant, which induces a constant I_{DS} condition. Therefore, equation (2) can be reexpressed with a bias-current, and further taking the channel conductivity ($\sigma = en\mu$) into account, yields

$$G_{ph} = \frac{1}{LW} \frac{1}{en} \tau_{trap} I_{DS}. \quad (5)$$

Likewise, devices observe the same irradiance \mathbb{I}_{in} rather than the same light power P_{in} . Including (5) and \mathbb{I}_{in} into equation (3) hence results in

$$I_{ph} = \frac{1}{E_{ph}} \frac{1}{n} \eta_{QE} \tau_{trap} \mathbb{I}_{in} I_{DS}, \quad (6)$$

and predicts a geometry-independent photocurrent. Note that n states the charge carrier density for electrons if positive and for holes if negative to account for the ambipolar graphene FET behavior.

In Figure 2 (c), the photocurrent of two devices close to the photocurrent saturation limited film thickness were compared. The two devices were fabricated independently, and the cQDs deposition method was varied between EHD printing and LbL spin coating as described in Figure 1 (b) and (c). I_{ph} was normalized by I_{DS} to account for contact resistances. The photoresponse shows a $1/n$ proportionality, and drops to zero at the Dirac point of graphene.

Although solid-state ligand exchanged cQD films are predominantly fabricated by a LbL approach in the literature, they do not necessarily result in a higher conductivity than a single-step ligand exchanged approach.³⁸ Accordingly, the devices with the EHD printed cQD films (single-step ligand exchange) demonstrate a slightly higher photoresponse of about a factor of 1.8. The ratio of the mobilities μ is about 1.9. Using equation (6), the photogating efficiency η_{Gph} was estimated from the experiments as shown in the bottom panel. The extracted η_{Gph} also takes the different wavelengths from the measurements (different first excitonic peaks, although the same cQD are used for the different devices) into account. The efficiency ratio is about 1.6 and similar to the I_{ph} and μ ratios. The photogating efficiency can further be expressed as

$$\eta_{Gph} = \eta_{trans}\eta_{abs}, \quad (7)$$

where η_{trans} describes the charge transfer efficiency, how well a photogenerated charge can be extracted from the cQD layer to graphene, and η_{abs} light absorption efficiency, how many e-h pairs are generated per incident photon.^{30,33,44} Furthermore, η_{abs} can be estimated to be in the range of 0.6 to 0.8. As the magnitude of η_{Gph} is in the order of 10^{-6} and one order of magnitude is lost to the absorption ($\eta_{abs} < 1$), there is only about one every 10^5 charge carriers that are extracted to graphene. Thus η_{trans} is a major source for improvement and stresses that a single-step ligand exchange is not a limiting factor.

Scaling of Pixel Dimensions

Next, the geometrical scaling of hybrid graphene – cQD phototransistors was investigated. All devices were fabricated on the same sample, and the cQD film was prepared by LbL spin coating to reduce device-to-device variations. First, equation (6) was validated by bias, irradiance, and frequency sweeps for devices with different L and a W of $5\ \mu\text{m}$. Figure 3 (a) shows the linear relation between the source-drain current I_{DS} and I_{ph} with a proportionality factor K_1 . The bias voltage was scaled according to $V_{DS} = |\vec{E}|L$ for comparable electric fields in the different devices. For better visualization, the measured source-drain current I_{DS} was normalized by its highest value $I_{DS,max}$. The inset shows each device's highest photocurrents $I_{ph,max}$ at $I_{DS,max}$. Every device was measured at the gate voltage where the highest photocurrent was observed in the p-doped region of graphene (red dashed line in Figure 2 (b)). The n-doped photocurrent maxima was experimentally not accessible as the LbL spin coating led to Dirac point voltages up to 70 V.

From equation (6), there is no length dependence expected, and all curves in Figure 3 (a) should lay on a single line. The inset shows that despite the applied comparable electric field condition across devices, I_{DS} still scales with L . This can be explained by a voltage drop over the contacts that becomes comparable to the voltage drop over the channel for smaller L , and thus $|\vec{E}|$ is not the same over the different channels despite the scaled V_{DS} . The contact resistance R_C is estimated to be in the range of about $0.6\ \text{k}\Omega$ per contact by performed transfer length method (TLM) measurements. Thus, the ratio of $2 \times R_C$ and the

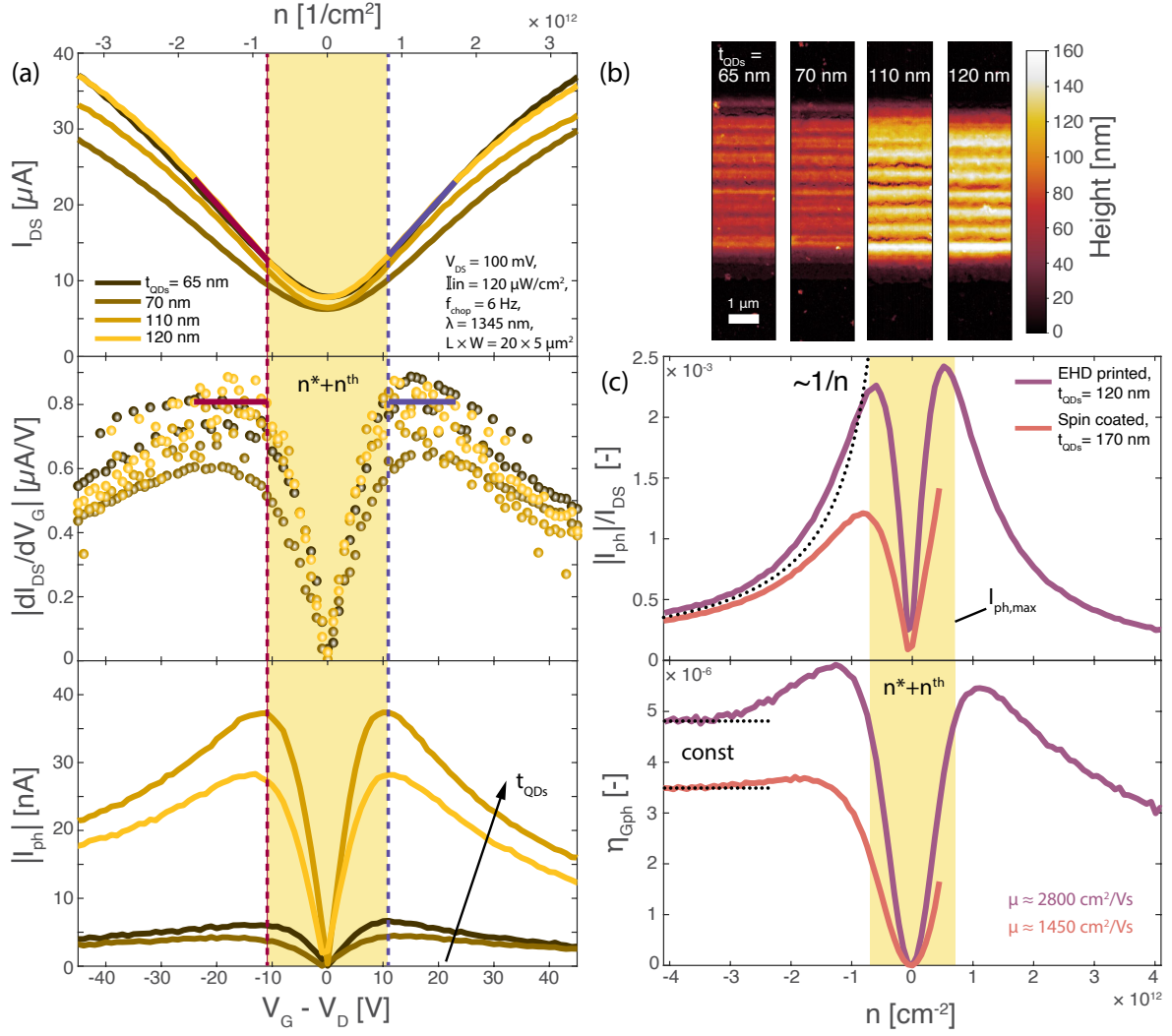


Figure 2: Photoresponse transfer characteristic and comparison of devices with EHD and LbL spin-coated films. (a) transfer characteristic of four devices with EHD PbS cQD film of different thicknesses. From top to down, the source-drain current I_{DS} , transconductance $g_m = dI_{DS}/dV_G$ and photocurrent I_{ph} from the same measurement were extracted. The gate voltage V_G is corrected by the Dirac point voltage V_D . g_m was derived from I_{DS} by a numerical derivative and is highlighted as dots to distinguish from the measured quantities. The dashed lines show the maximum I_{ph} in the p- (red) and n-doped (blue) regions of graphene. The solid red and blue line in g_m and I_{DS} indicates the region of about constant maxima of g_m and is displayed for the device with $t_{QDs} = 120$ nm only. (b) AFM images of the characterized devices in (a), showing the thickness t_{QDs} of cQD films on top of graphene. (c) cross-comparison of two devices with EHD printed and LbLs spin coated cQDs films. I_{ph} (top panel) was normalized by I_{DS} to account for contact resistance and bias conditions V_{DS} of 100 (EHD) and 200 mV (LbL). Devices were measured at a wavelength λ matching the respective first excitonic peaks of 1345 (EHD) and 1550 nm (LbL), and $I_{in} = 120$ $\mu W/cm^2$. The bottom panel shows the two devices' derived photogating efficiency η_{Gph} . Yellow shading illustrates where the highest photocurrent I_{ph} has been found. The shaded region might originate from random potential in graphene around the Dirac point $n^* + n^{th}$, where a gate can not control the conductivity of graphene.

channel resistance R_{Ch} become comparable ($2R_C/R_{Ch} \geq 0.5$) for devices with $L < 5$ μm . Reversibly, the contact resistance can be estimated from the spread of the I_{ph} vs. I_{DS} curves assuming the same $|\vec{E}|$ over the channel leads to the same I_{DS} . This also results in $R_C \approx 0.6$

kΩ. With the fact that I_{ph} is linearly proportional to I_{DS} , this confirms the origin of the I_{ph} spread from contact limitations.

In Figure 3 (b), irradiance sweeps were performed for the same set of devices. This I_{ph} - I_{in} relation is linear with a proportionality factor K_2 . K_2 is related to the responsivity by $R = \frac{K_2}{LW}$. As the curves follow a linear fit (dotted line), the detectors were operated in the linear dynamic regime ($R = const$), reaching responsivity values about 300 A/W for $|\vec{E}| = 10$ kV/m and $f_{chop} = 6$ Hz. The inset highlights the noise equivalent irradiance (NEI) for the different devices in the range of 1 to 10 $\mu\text{W}/\text{cm}^2$. The specific detectivity can be calculated by^{30,32}

$$D^* = \frac{\sqrt{LW} \sqrt{\Delta f}}{NEP} = R \frac{\sqrt{LW} \sqrt{\Delta f}}{I_{noise}}. \quad (8)$$

$NEP = NEI \times LW$ is the noise equivalent power, Δf the frequency bandwidth, and I_{noise} the noise current. The resulting detectivities are about 2×10^8 Jones at 6 Hz and with $\Delta f = 0.026$ Hz (equivalent noise bandwidth of lock-in measurement).

Figure 3 (c) shows the frequency response of the investigated devices. The light chopping frequency f_{chop} was varied between 5 and 200 Hz. A fit to data relates $I_{ph} = K_3 f^\alpha$ dependence, where K_3 is a proportionality constant. The curves follow $\alpha = -0.5 (\pm 0.1)$ up to frequencies of about 160 Hz. A differing photocurrent dynamics can be observed for the 1 μm channel length device (dark brown). Around 70 Hz, the trend deviates from the $\alpha = -0.5$ as I_{ph} increases with f_{chop} before it drops eventually.

The chopping frequency is defined over which period τ_{chop} the detector sees the light. Thus, it probes τ_{trap} of the cQD film. Previous experiments have shown that at least two trapping times can be present underlying the photocurrent dynamics.^{29,45,46} In analogy to low frequency $1/f$ noise⁴⁷, the frequency response might originate from an envelope of individual Lorentzian shaped trap state contributions. Thus, the slope of the envelope α is a cQD film-dependent quantity and depends on the specific film treatment as it varies across the literature (values between -0.1 to -2).^{11,25,45} Within this frame, a possible explanation of the rise of I_{ph} around 130 Hz might be the quenched escape rate from such a trap, as new carriers are excited before the trapped ones escape. Consequently, the traps might be constantly populated, and newly photoexcited e-h pairs can escape without being slowed down from those traps, leading to higher photocurrents. The energy depth of such a trap i can be estimated by $\Delta E_{trap,i} = -kT \ln(\tau_0/\tau_{trap,i})$, with k the Boltzmann constant, and T the temperature.⁴⁸ The free charge carrier lifetime τ_0 is the recombination time of a charge carrier contributing to the photocurrent, excluding the time it spends in a trap. For $1/\tau_{trap,i} = 130$ Hz an energy depth of $\Delta E_{trap,i} \approx 250$ meV can be estimated, that corresponds to previously found surface trap state energies for PbS cQD films between 100 to 300 meV.⁴⁹ For a spin coated film, this trap state is expected to be equally distributed throughout the film. However, in Figure 3 (c), the trap appears for the device with a channel length of 1 μm , and might be explained by the modulation of the trap in the vicinity of the source and drain electrodes.

Figure 3 (d) shows the bias current normalized power spectral density of the measured

noise current. The curves show a low frequency $1/f$ -noise dependence as typically reported⁴⁷ for graphene FETs. The measurements were performed in the dark and at the same scaled bias condition $V_{DS} = |\vec{E}|L$. Fit to the curves reveal a mean exponent of -1.01 ± 0.02 . The inset shows the derived specific detectivity D^* using equation (8) and taking the photocurrents from Figure 3 (c) into account. The yellow line ($L = 20 \mu\text{m}$) has a near constant D^* up to a frequency of 200 Hz and represents most of the investigated devices. On the other hand, the dark brown curve ($L = 1 \mu\text{m}$) shows an increase of D^* up to 130 Hz, possibly due to quenched trapping sites leading to a rise of the photocurrent. The D^* values of about 2×10^8 Jones fit well with the estimation from NEP found in Figure 3 (b).

All the three introduced proportionality factors K_j are related to η_{Gph} and can be expressed from equation (6) as

$$\eta_{Gph} = nE_{ph} \frac{1}{\tau_{trap}} \frac{1}{\mathbb{I}_{in}} \frac{1}{I_{DS}} I_{ph}. \quad (9)$$

The decay time τ_{trap} describes how long it takes to recover the dark current once the light is turned off. Thus, τ_{trap} defines the detector's maximum reachable photogain G_{ph} . To describe the experimentally observed $I_{ph} \sim f^\alpha$ dependence, and the fact that f_{chop} probes $\tau_{trap,i}$, the chopping frequency can be modeled by $\tau_{trap} = \beta f_{chop}^\alpha$. Here, β is introduced to formally correct the unit discrepancy arising from the fitting constant α . As a result, the estimation of η_{Gph} can be performed with f_{chop} , \mathbb{I}_{in} , and I_{DS} sweeps. Using the proportionality factors K_j from Figure 3 (a) to (c), the photogating efficiency was estimated in Figure 3 (d). η_{Gph} yield a channel length dependence and similar values across the different measurements. Furthermore, the values of $\sim 10^{-6}$ are compatible with the observation in Figure 2 (c). A similar decreasing trend was observed for both g_m and η_{Gph} towards smaller L . Previously, contacting metals have been found to dope ~ 500 nm into the graphene channel⁵⁰, thus reducing the effective gateable length of the channel, and limiting g_m for small devices. As both g_m (back gate) and η_{Gph} (photogate) are related to the gating of the graphene channel, the same loss of gateable channel length might be the cause for decreasing η_{Gph} with smaller L .

Next, the scaling of the photoresponse by L and W was investigated as seen in Figure 4. For that devices with L (number of devices) of 0.5 ($\times 5$), 1 ($\times 6$), 2.5 ($\times 4$), 5 ($\times 5$), 10 ($\times 3$), and 20 μm ($\times 7$) with a width of $W = 5 \mu\text{m}$ were measured for the L -scaling. For W -scaling W (number of devices) of 0.5 ($\times 3$), 1 ($\times 5$), 2.5 ($\times 4$) and 5 μm ($\times 7$) with a $L = 20 \mu\text{m}$ were characterized. All the devices were on the same chip and had identical cQD film properties, allowing for a cross-comparison. The quantities I_{ph} , I_{DS} , n were extracted from gate sweeps as described in Figure 2 (a). The values were taken at respective maximum photocurrent points in the p-doped region of graphene. As the photoresponse is proportional to I_{DS} , V_{DS} was scaled for a comparable current condition according to $I_{DS} \sim W \frac{V_{DS}}{L}$.

In Figure 4 (a), G_{ph} scaling by L (top) and W (bottom) is presented. A fit to the data (black dotted line) shows the $1/L$ trend and agrees with the prediction from equation (5). The horizontal dotted line indicates the mean value in that range. The scaling law breaks down around 1.5 μm (orange shaded region), where the total graphene FET resistance R_T is

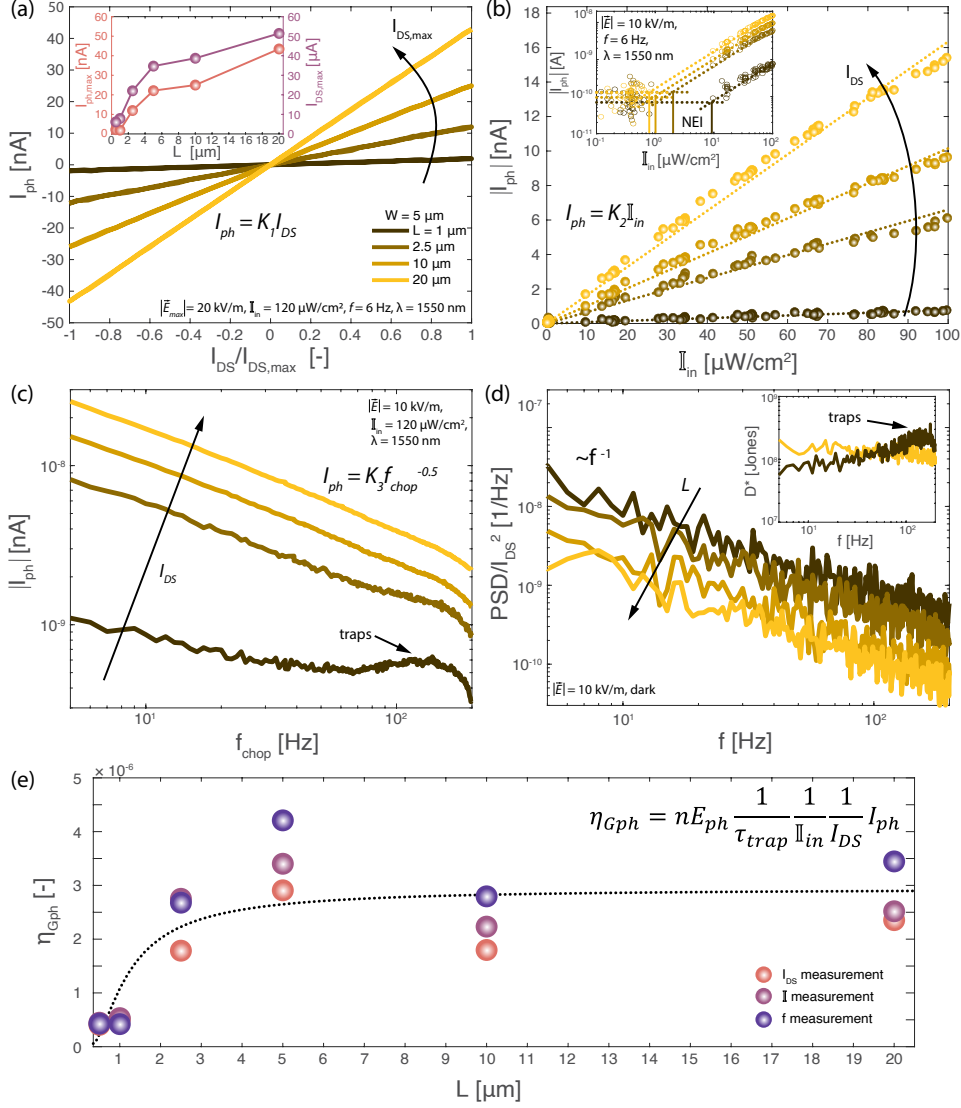


Figure 3: Bias, irradiance, and frequency dependence of photocurrent for a set of devices with $W = 5 \mu\text{m}$, varying L , and LbL spin coated cQDs PbS film of $t_{QDS} \approx 170 \text{ nm}$. (a) Linear dependence of $I_{ph} = K_1 I_{DS}$. Bias voltage V_{DS} range was scaled to reach a maximum of $|\vec{E}_{max}| = 20 \text{ kV/m}$. I_{DS} was normalized by its maximum value for better illustration. The highest measured I_{ph} and I_{DS} for an extended set of devices are shown in the inset. (b) Linear dependence of $I_{ph} = K_2 I_{in}$. The dotted lines show linear least squares fit (LSQ) through the data. Inset shows the noise equivalent irradiance (NEI) in the log-log plot. (c) Frequency response of I_{ph} by sweeping the light chopping frequency f_{chop} . $I_{ph} = K_3 f_{chop}^\alpha$, with $\alpha = -0.5 \pm 0.1$ estimated from LSQ fit to log-log plot. (d) power spectral density (PSD) of the noise current I_{noise} , measured in dark. PSD was normalized by the measured I_{DS} . LSQ fit the log-log plots show a mean exponent of -1.01 ± 0.02 to the frequency f . (e) Photogating efficiency η_{Gph} estimate based on LSQ fits giving proportionality factors K_j from (a),(b), and (c). The full formula is given in the figure. τ_{trap} was estimated as $1/\sqrt{6}$ in agreement with fits in (c). In (b),(c), and (d) V_{DS} was scaled according to $|\vec{E}| = 10 \text{ kV/m}$. Note that measurements were performed on an extended set of devices including L of 0.5, 1, 2.5, 5, 10, 20 μm , but for clarity, only a distinct set is plotted in (a) to (d). Applied gate voltage of $V_G = 58 \text{ V}$ for devices with L of 0.5, 2.5, 10 μm and $V_G = 48 \text{ V}$ for L of 1, 5, 20 μm for all the measurements.

about $2 \text{ k}\Omega$. This is comparable to the contact resistance of $1.2 \text{ k}\Omega$ (600Ω per contact) and thus points to a current injection limitation at the specified biasing condition. The W -scaling

follows a predicted $1/W$ trend over the evaluated region. As the W -scaling devices have a $L = 20\ \mu\text{m}$, the smallest resistance for the $W = 5\ \mu\text{m}$ is about $8\ \text{k}\Omega$ such that no current injection limitation is observed.

Figure 4 (b) depicts the scaling of photoresponsivity R . The responsivity was normalized by n/I_{DS} to account for device-to-device variations (different residual doping levels) and contact resistance. R follows also a $1/L$ -scaling law. Although I_{ph} is independent on geometry for constant \mathbb{I}_{in} , $P_{in} = \mathbb{I}_{in}LW$ and thus

$$R = \frac{I_{ph}}{\mathbb{I}_{in}LW}. \quad (10)$$

The breakdown of the scaling law, however, exceeds the current injection limited region caused by contacts (yellow shaded) and extends up to $\sim 3\ \mu\text{m}$. The inset shows the normalization factor additionally accounting for η_{Gph} . As η_{Gph} is introduced, the red shaded area appears, thus being responsible for an additional length limitation to the scaling. The bottom panel shows the same normalized R for the W -scaling. In fact, as for the gain, there is a good agreement for the $1/W$ scaling observed over the investigated width scale. Moreover, the normalization factor, including η_{Gph} , shows a constant trend. This highlights that η_{Gph} might be similarly affected by reduced gateable channel lengths due to metal doping, as mentioned for g_m above.

Finally, the influence of scaling on the noise and specific detectivity D^* was investigated in Figure 4 (c). From I_{DS}^2 normalized PSD spectra as shown in Figure 3 (d), the values at 6 Hz were extracted for every device. The measurements were performed in dark and at the same gate voltage where the maximum photocurrent was extracted previously. The dotted lines show fits through the mean values of each length or width, whereas the purple shading indicates the standard deviation. The fits suggest a $1/\sqrt{L}$ and $1/W$ dependence for the characterized devices. For the L -scaling, the distribution of points increases as L gets smaller, whereas the W -scaling has an overall smaller spread of the data. The inset shows derived D^* about 3×10^8 Jones, using the photoresponse shown in (b).

Low frequency $1/f$ noise in GFETs is primarily attributed to electrostatic fluctuations arising from trap states at the oxide interface and leads to conductivity fluctuations in the channel.^{47,51} Conductivity σ is related to the product of $n\mu$. Hence, the two main models that describe $1/f$ noise are based on Δn (McWorther's model) or $\Delta\mu$ (Hooge's law) fluctuations.^{47,52} Both models predict a $1/LW$ dependence of noise in the FET channels.⁵² Accordingly, a volume scaling was experimentally verified for metallic break junctions to hold in the diffusive transport regime.⁵³ For graphene FETs, however, the $1/LW$ scaling has been found to experimentally not describe the data in full detail.⁵⁴ Being restricted to a surface only, graphene is very sensitive to its environment. Thus, perturbations to the channel such as bilayers⁵⁵, contacts^{54,56}, and environmental exposure⁵⁴ are altering the electrostatic screening potential of the channel and influence the low-frequency $1/f$ noise. Like the photoresponse, though, reducing L is pronouncing the contact effects. Hence, an increasing spread for smaller

L channels is observed. In addition, possible regions of double layers due to non-ideal CVD graphene growth and the additional current path through the cQD can thus be the reason for a deviation from an overall $1/LW$ trend observed in the PSDs.

Expanding the demonstrated photocurrent characteristics of equation (6) into the detectivity yields

$$D^* = \frac{1}{n} \frac{1}{E_{ph}} \tau_{trap} \eta_{QE} \frac{1}{\sqrt{LW}} \frac{1}{\sqrt{PSD/I_{DS}^2}}. \quad (11)$$

If now $\sqrt{PSD/I_{DS}^2} \sim 1/\sqrt{LW}$, there is no geometrical dependence expected in D^* , which is consistent with the performed measurements. It is important to mention that the experimentally determined D^* values between 10^8 to 10^9 Jones are around four orders of magnitude lower than the highest values found in the literature¹⁶ of 10^{13} Jones. The difference can be explained mainly by two factors from equation (11). First, the difference is in the found η_{Gph} range. As η_{Gph} does not differ much for devices with EHD printed (single step ligand exchange) and a LbL spin coated cQD films, the interface between graphene and cQD film limits most likely the charge transfer. CVD graphene processing is prone to defects and residuals from the growth and device fabrication. On the contrary, the highest D^* values were reached with exfoliated single-crystal graphene. Second, τ_{trap} defines the maximum reachable gain and is related to the photocurrent dynamics (I_{ph} to f_{chop} relation). Preserving the I_{ph} magnitude for increasing f_{chop} leads to increasing D^* due to lower $1/f$ noise in the channel as demonstrated in Figure 3 (c) and (d).

Conclusion

Here, the scaling of hybrid graphene-PbS cQD phototransistors with channel length L , width W , and cQD film thickness t_{QDs} was experimentally demonstrated. The photocurrent I_{ph} was found to be independent of L and W but increased with t_{QDs} . Instead, the photogain G_{ph} and responsivity R scaled with $1/LW$. Although a $1/L^2$ dependence can be derived for G_{ph} , this neglects increasing channel currents with $I_{DS} \sim V_{DS}W/L$. Relating G_{ph} to I_{DS} leads to the $1/LW$ relation. For R , on the contrary, the geometrical dependence is evolving from a constant irradiance $\mathbb{I}_{in} = P_{in}/LW$, rather than a constant light power P_{in} seen by the detector. The L scaling broke down for $L < 3 \mu\text{m}$ due to contact metal contributions (contact resistance and channel doping). Although specific detectivity is $D^* \sim R$, the found values in the range between 10^8 to 10^9 Jones ($\lambda = 1550 \text{ nm}$, $f = 6 \text{ Hz}$, room temperature) were independent on geometry. This is due to increasing noise currents for smaller dimensions. The photoresponse dependency on back gate voltage V_G , bias I_{DS} , irradiance \mathbb{I}_{in} , and light chopping frequency f_{chop} were analyzed. A derived photogating efficiency η_{Gph} of $\sim 10^{-6}$ from those measurements pointed to a cQD-graphene interface limited charge transfer as a source for further photoresponse improvement.

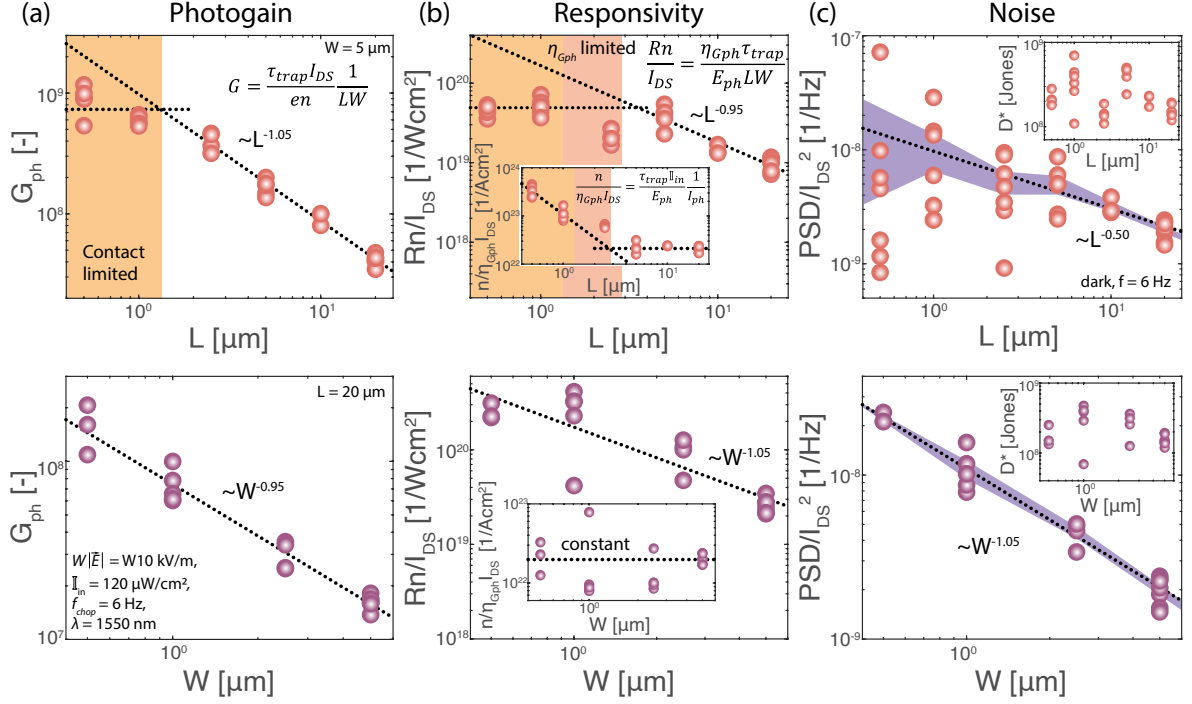


Figure 4: Length and width scaling of photoresponse. (a) photogain G_{ph} scaling. LSQ fits exponents for L of 1.05 ± 0.025 and for W of 0.95 ± 0.025 (dotted black line). The orange-shaded region highlights where the L -scaling breaks down as contact resistances become comparable to device channel resistances. (b) Responsivity R scaling. R was normalized by charge carrier density n (different residual doping levels) and I_{DS} (contact resistance). An exponent for L of 0.95 ± 0.05 and W of 1.05 ± 0.1 was fitted by LSQ. The L -scaling shows contact limited (orange) and η_{QE} limited range. The inset shows the η_{QE} extended normalization factor for R , where the red-shaded region becomes visible. (c) power spectral density (PSD) of the noise current I_{noise} . The noise was measured in dark, and PSD was normalized by the measured I_{DS}^2 . LSQ fits exponents of 0.502 ± 0.02 for L -scaling and 1.05 ± 0.03 (black dashed line). Purple shading shows the standard deviation of the mean values. Specific detectivity D^* estimates between 10^8 to 10^9 are shown in the insets. The bias voltage V_{DS} was scaled for a constant current condition according to $I_{DS} \sim W \frac{V_{DS}}{L}$. All values for (a) and (b) are extracted from maximum I_{ph} points acquired in gate voltage sweeps, at a wavelength $\lambda = 1550 \text{ nm}$, $I_{in} = 120 \mu\text{W/cm}^2$, and $f_{chop} = 6 \text{ Hz}$. (c) was measured at the same V_G values as in (a) and (b). The dotted horizontal lines indicate the mean values of the respective data sets.

Methods

Graphene Growth

CVD graphene was grown on commercial copper foil (Foil 2017, No. 46365, Alfa Aesar). The Cu-foil was first sonicated in acetone (15 min) and rinsed with deionized (DI) water. The foil was then immersed in nitric acid HNO_3 (30 min), twice sonicated in DI-water (1 min), immersed in ethanol (1 min), and blow-dried with N_2 . The Cu-foil was annealed in H_2 (20 sccm H_2 and 200 sccm Ar mixture) at 1000°C and a pressure of $< 1 \text{ mbar}$ for 70 min in a furnace. The graphene was grown from 0.04 sccm methane CH_4 for 21 min at 1000°C and a pressure of 110 mbar, subsequently cooled down by opening the temperature shielding.

Graphene field effect transistor Fabrication

A p-Si substrate with 285 nm chlorinated dry thermal SiO_2 was prepatterned with contacts. The contacts were fabricated by e-beam-assisted thermal evaporation of Ti/Au (5/40 nm) on a photolithographically defined resist (AZ5214E). PMMA 50K-protected graphene was prepared for wet transfer by Cu-etching in commercial Transene etchant (1 h), rinsed with DI water, left floating on hydrochloric acid (5 min), and re-rinsed with DI

water. Graphene was transferred on the pre-patterned p-Si substrate from DI water, dried on a hotplate, and put into a vacuum (~ 60 h). Graphene channels were O₂-plasma etched using a Cu-mask, followed by Cr/Au top-contacts (2/40 nm), both defined by e-beam lithography (PMMA 50K/PMMA 950K).

PbS cQD Film Fabrication

PbS QDs were synthesized following Hines et al.⁵⁷ with slight adaptations as described in detail previously²⁹. For electrohydrodynamic nanoprinting (EHD), the PbS cQD were redispersed in n-tetradecane with a concentration of 40 mg/ml and filtered with 0.1 μ m PTFE syringe filter. Printing nozzles with openings between 2 to 3 μ m were fabricated by pulling glass capillaries (World Precision Instruments TW100-4) and subsequent coating Ti/Au (5/50 nm). For the printing, the nozzle was brought in ~ 5 μ m proximity to the sample and an AC voltage of 280 V (250 Hz) was applied between sample and nozzle. The structures were printed with a stage speed of 6 μ m/s, line-spacing about 500 nm, and subsequent overprinting was oriented in a staggered fashion. The EHD printing system used here was previously described in more detail.⁵⁸ A single-step ligand exchange was performed by overnight soaking the cQD films in 2 vol% ethane-1,2-dithiol (EDT) in acetonitrile. Subsequently, the samples were rinsed in acetonitrile and dried with N₂.

For the layer-by-layer (LbL) prepared film, the PbS cQDs were redispersed in octane with a concentration of 20 mg/ml. A layer of PbS cQDs was spin-coated (2500 rpm, 45 s), subsequently a drop of 2 vol% ethane-1,2-dithiol (EDT) in acetonitrile was placed for 30 s before spinning the sample dry, and followed by one drop of acetonitrile and one drop of octane while sample was spinning (2500 rpm, 45 s). The steps were repeated six times for a ~ 170 nm film thickness.

Before film fabrication, the PbS cQDs were characterized by UV-Vis spectroscopy (Jasco V-670). The fabricated PbS cQD films were analyzed by AFM (Bruker Dimension ICON 3), and the device cross-section was investigated by FIB-SEM (FEI Helios NanoLab G3 UC).

Device Characterization

The GFET were electrical characterization before PbS cQD film deposition in a two-probe configuration (Keithley 4200-SCS semiconductor characterization system). The field-effect mobility $\mu = \frac{L}{WV_{DS}C_G} \frac{dI_{DS}}{dV_G}$ was estimated by linear least squares fit (LSQ) to transfer curves (I_{DS} vs. V_G). The contact resistance was estimated by the transfer length method (TLM).

To characterize the photoresponse, a broadband light source (Thorlabs, SLS201) was modulated with a chopper (Thorlabs, MC2000B-EC) and focused onto a monochromator (Princeton Instruments, SpectraPro HRS-300 spectrometer with grating 150 G/mm, blaze 0.8 μ m). Subsequent long-pass filters attenuated the higher spectral orders (400, 600, 800, 1200, 1900 nm) at the monochromator exit. The light was collimated with a lens and split with a 50/50 Polkadot beamsplitter. Onto one end, a reference detector (Gentec, UM-9B-L) was placed, and the light irradiance was determined by a lock-in amplifier (Stanford Research System, SR865A). Onto the other light path end, the samples were placed into an optically accessible cryostat (JANIS ST-100) with a quartz glass window. Gate voltage and source-drain bias were applied with SMUs (Keithley, 2614B and 2450). The photovoltage was measured over a shunt resistance of 1 k Ω with lock-in amplifiers (Stanford Research System, SR860).

Noise currents were measured in the dark with a battery-powered trans-impedance amplifier (Stanford Research Systems, SR570). The signal was low pass filtered (10 kHz) and subsequently acquired with a data acquisition board (National Instruments, USB6341) at a sampling rate of 500 kHz. The DC offset was removed for the power spectral densities estimates, and 10 \times one-second-long time traces were averaged.

All measurements were performed at room temperature and vacuum ($4 \cdot 10^{-7}$ mbar). The line frequency of 50 Hz and its harmonic 150 Hz were removed from all the frequency-dependent measurements. The measurements were repeated throughout the study duration for a selected set of devices (~ 21 days). In between the measurements, the samples were taken out of the measurement setup, rebonded in atmosphere, and placed

back in the measurement setup. The measurements were reproducible with a maximal deviation of $\sim 30\%$. A device of each dimension was measured before the next one with the same dimension was investigated to reduce the influence of possible variation from sample alignment or degradation on the study outcome.

Acknowledgements

The authors thank FIRST-Lab (Center for Micro- and Nanoscience) at ETH Zurich for access to the clean-room and the Swiss National Science Foundation (SNSF, project no. 200021 182790) for financial support.

Author Contribution

G.K. and I.S. conceived the study and planned the experiments. G.K. fabricated the samples, performed the measurements and analyzed the data. P.R. performed the EHD printing with supervision by D.P. E.W. performed the FIB-SEM images. D.D. synthesized PbS colloidal QDs. R.F. grew graphene. G.K., I.S. and M.C. discussed the data. I.S., M.C., M.K, D.P. initiated and supervised the project. G.K. wrote the manuscript with inputs and discussions from all authors.

References

- [1] M. V. Kovalenko, L. Manna, A. Cabot, Z. Hens, D. V. Talapin, C. R. Kagan, V. I. Klimov, A. L. Rogach, P. Reiss, D. J. Milliron, P. Guyot-Sionnest, G. Konstantatos, W. J. Parak, T. Hyeon, B. A. Korgel, C. B. Murray, and W. Heiss, "Prospects of nanoscience with nanocrystals," *ACS Nano*, vol. 9, no. 2, pp. 1012–1057, 2015.
- [2] H. Lu, G. M. Carroll, N. R. Neale, and M. C. Beard, "Infrared Quantum Dots: Progress, Challenges, and Opportunities," *ACS Nano*, vol. 13, no. 2, pp. 939–953, 2019.
- [3] X. Tang, M. M. Ackerman, and P. Guyot-Sionnest, "Acquisition of Hyperspectral Data with Colloidal Quantum Dots," *Laser and Photonics Reviews*, vol. 13, no. 11, 2019.
- [4] X. Tang, M. M. Ackerman, M. Chen, and P. Guyot-Sionnest, "Dual-band infrared imaging using stacked colloidal quantum dot photodiodes," *Nature Photonics*, vol. 13, no. 4, pp. 277–282, 2019.
- [5] X. Tang, M. Chen, A. Kamath, M. M. Ackerman, and P. Guyot-Sionnest, "Colloidal Quantum-Dots/Graphene/Silicon Dual-Channel Detection of Visible Light and Short-Wave Infrared," *ACS Photonics*, vol. 7, no. 5, pp. 1117–1121, 2020.
- [6] J. Gao, S. C. Nguyen, N. D. Bronstein, and A. P. Alivisatos, "Solution-Processed, High-Speed, and High-Quantum-Efficiency Quantum Dot Infrared Photodetectors," *ACS Photonics*, vol. 3, no. 7, pp. 1217–1222, 2016.
- [7] M. Biondi, M. J. Choi, Z. Wang, M. Wei, S. Lee, H. Choubisa, L. K. Sagar, B. Sun, S. W. Baek, B. Chen, P. Todorović, A. M. Najarian, A. Sedighian Rasouli, D. H. Nam, M. Vafaie, Y. C. Li, K. Bertens, S. Hoogland, O. Voznyy, F. P. García de Arquer, and E. H. Sargent, "Facet-Oriented Coupling Enables Fast and Sensitive Colloidal Quantum Dot Photodetectors," *Advanced Materials*, vol. 33, no. 33, 2021.
- [8] M. Vafaie, J. Z. Fan, A. Morteza Najarian, O. Ouellette, L. K. Sagar, K. Bertens, B. Sun, F. P. García de Arquer, and E. H. Sargent, "Colloidal quantum dot photodetectors with 10-ns response time and 80% quantum efficiency at 1,550 nm," *Matter*, vol. 4, no. 3, pp. 1042–1053, 2021.
- [9] A. A. Bessonov, M. Allen, Y. Liu, S. Malik, J. Bottomley, A. Rushton, I. Medina-Salazar, M. Voutilainen, S. Kallioinen, A. Colli, C. Bower, P. Andrew, and T. Ryhänen, "Compound Quantum Dot-Perovskite Optical Absorbers on Graphene Enhancing Short-Wave Infrared Photodetection," *ACS Nano*, vol. 11, no. 6, pp. 5547–5557, 2017.
- [10] X. Tang, M. M. Ackerman, G. Shen, and P. Guyot-Sionnest, "Towards Infrared Electronic Eyes: Flexible Colloidal Quantum Dot Photovoltaic Detectors Enhanced by Resonant Cavity," *Small*, vol. 15, no. 12, 2019.
- [11] E. O. Polat, G. Mercier, I. Nikitskiy, E. Puma, T. Galan, S. Gupta, M. Montagut, J. J. Piqueras, M. Bouwens, T. Durduran, G. Konstantatos, S. Goossens, and F. Koppens, "Flexible graphene photodetectors for wearable fitness monitoring," *Science Advances*, vol. 5, no. 9, 2019.
- [12] J. Kim, S.-M. Kwon, Y. K. Kang, Y.-H. Kim, M.-J. Lee, K. Han, A. Facchetti, M.-G. Kim, and S. K. Park, "A skin-like two-dimensionally pixelized full-color quantum dot photodetector," *Science Advances*, vol. 5, p. eaax8801, aug 2023.
- [13] J. S. Steckel, E. Josse, A. G. Pattantyus-Abraham, M. Bidaud, B. Mortini, H. Bilgen, O. Arnaud, S. Allegret-Maret, F. Saguin, L. Mazet, S. Lhostis, T. Berger, K. Haxaire, L. L. Chapelon, L. Parmigiani, P. Gouraud, M. Brihoum, P. Bar, M. Guillermet, S. Favreau, R. Duru, J. Fantuz, S. Ricq, D. Ney, I. Hammad, D. Roy, A. Arnaud, B. Vianne, G. Nayak, N. Virollet, V. Farys, P. Malinge, A. Tournier, F. Lalanne, A. Crocherie, J. Galvier, S. Rabary, O. Noblanc, H. Wehbe-Alaouse, S. Acharya, A. Singh, J. Meitzner, D. Aher, H. Yang, J. Romero, B. Chen, C. Hsu, K. C. Cheng, Y. Chang, M. Sarmiento, C. Grange, E. Mazaleytrat, K. Rochereau, Jonathan Steckel, E. Josse, A. G. Pattantyus-Abraham, M. Bidaud, B. Mortini, H. Bilgen, O. Arnaud, J. S. Steckel, E. Josse, A. G. Pattantyus-Abraham, M. Bidaud, B. Mortini, H. Bilgen, O. Arnaud, S. Allegret-Maret, F. Saguin, L. Mazet, S. Lhostis, T. Berger, K. Haxaire, L. L. Chapelon, L. Parmigiani, P. Gouraud, M. Brihoum, P. Bar, M. Guillermet, S. Favreau, R. Duru, J. Fantuz, S. Ricq, D. Ney, I. Hammad, D. Roy, A. Arnaud, B. Vianne, G. Nayak, N. Virollet, V. Farys, P. Malinge, A. Tournier, F. Lalanne, A. Crocherie, J. Galvier, S. Rabary, O. Noblanc, H. Wehbe-Alaouse, S. Acharya, A. Singh, J. Meitzner, D. Aher, H. Yang, J. Romero, B. Chen, C. Hsu, K. C. Cheng, Y. Chang, M. Sarmiento,

- C. Grange, E. Mazaleyrat, and K. Rochereau, "1.62 μ m Global Shutter Quantum Dot Image Sensor Optimized for Near and Shortwave Infrared," *Technical Digest - International Electron Devices Meeting, IEDM*, pp. 518–521, 2021.
- [14] C. Gréboval, A. Chu, D. V. Magalhaes, J. Ramade, J. Qu, P. Rastogi, A. Khalili, S. S. Chee, H. Aubin, G. Vincent, S. Bals, C. Delerue, and E. Lhuillier, "Ferroelectric Gating of Narrow Band-Gap Nanocrystal Arrays with Enhanced Light-Matter Coupling," *ACS Photonics*, vol. 8, no. 1, pp. 259–268, 2021.
- [15] T. H. Dang, C. Abadie, A. Khalili, C. Gréboval, H. Zhang, Y. Prado, X. Z. Xu, D. Gacemi, A. Descamps-Mandine, S. Ithurria, Y. Todorov, C. Sirtori, A. Vasanelli, and E. Lhuillier, "Broadband Enhancement of Mid-Wave Infrared Absorption in a Multi-Resonant Nanocrystal-Based Device," *Advanced Optical Materials*, vol. 10, no. 9, 2022.
- [16] G. Konstantatos, M. Badioli, L. Gaudreau, J. Osmond, M. Bernechea, F. P. G. De Arquer, F. Gatti, and F. H. Koppens, "Hybrid graphene–quantum dot phototransistors with ultrahigh gain," *Nature Nanotechnology*, vol. 7, no. 6, pp. 363–368, 2012.
- [17] Z. Sun, Z. Liu, J. Li, G. A. Tai, S. P. Lau, and F. Yan, "Infrared photodetectors based on CVD-grown graphene and PbS quantum dots with ultrahigh responsivity," *Advanced Materials*, vol. 24, no. 43, pp. 5878–5883, 2012.
- [18] D. Kufer, I. Nikitskiy, T. Lasanta, G. Navickaite, F. H. Koppens, and G. Konstantatos, "Hybrid 2D-0D MoS₂-PbS quantum dot photodetectors," *Advanced Materials*, vol. 27, no. 1, pp. 176–180, 2015.
- [19] D. Kufer, T. Lasanta, M. Bernechea, F. H. Koppens, and G. Konstantatos, "Interface Engineering in Hybrid Quantum Dot-2D Phototransistors," *ACS Photonics*, vol. 3, no. 7, pp. 1324–1330, 2016.
- [20] O. Özdemir, I. Ramiro, S. Gupta, and G. Konstantatos, "High Sensitivity Hybrid PbS CQD-TMDC Photodetectors up to 2 μ m," *ACS Photonics*, vol. 6, no. 10, pp. 2381–2386, 2019.
- [21] B. Kundu, O. Özdemir, M. Dalmases, G. Kumar, and G. Konstantatos, "Hybrid 2D-QD MoS₂-PbSe Quantum Dot Broadband Photodetectors with High-Sensitivity and Room-Temperature Operation at 2.5 μ m," *Advanced Optical Materials*, vol. 9, no. 22, 2021.
- [22] H. T. Choi, J. H. Kang, J. Ahn, J. Jin, J. Kim, S. Park, Y. H. Kim, H. Kim, J. D. Song, G. W. Hwang, S. Im, W. Shim, Y. T. Lee, M. C. Park, and D. K. Hwang, "Zero-Dimensional PbS Quantum Dot-InGaZnO Film Heterostructure for Short-Wave Infrared Flat-Panel Imager," *ACS Photonics*, vol. 7, no. 8, pp. 1932–1941, 2020.
- [23] S. Ahn, W. Chen, M. A. Moreno-Gonzalez, M. Lockett, J. Wang, and O. Vazquez-Mena, "Enhanced Charge Transfer and Responsivity in Hybrid Quantum Dot/Graphene Photodetectors Using ZnO as Intermediate Electron-Collecting Layer," *Advanced Electronic Materials*, vol. 6, no. 6, 2020.
- [24] S. Ahn and O. Vazquez-Mena, "Measuring the carrier diffusion length in quantum dot films using graphene as photocarrier density probe," *Journal of Chemical Physics*, vol. 156, no. 2, 2022.
- [25] I. Nikitskiy, S. Goossens, D. Kufer, T. Lasanta, G. Navickaite, F. H. Koppens, and G. Konstantatos, "Integrating an electrically active colloidal quantum dot photodiode with a graphene phototransistor," *Nature Communications*, vol. 7, no. 1, 2016.
- [26] M. J. Grotevent, C. U. Hail, S. Yakunin, D. Bachmann, M. Calame, D. Poulidakos, M. V. Kovalenko, and I. Shorubalko, "Colloidal HgTe Quantum Dot/Graphene Phototransistor with a Spectral Sensitivity Beyond 3 μ m," *Advanced Science*, vol. 8, no. 6, 2021.
- [27] Z. Ni, L. Ma, S. Du, Y. Xu, M. Yuan, H. Fang, Z. Wang, M. Xu, D. Li, J. Yang, W. Hu, X. Pi, and D. Yang, "Plasmonic Silicon Quantum Dots Enabled High-Sensitivity Ultrabroadband Photodetection of Graphene-Based Hybrid Phototransistors," *ACS Nano*, vol. 11, no. 10, pp. 9854–9862, 2017.
- [28] M. J. Grotevent, C. U. Hail, S. Yakunin, D. N. Dirin, K. Thodkar, G. Borin Barin, P. Guyot-Sionnest, M. Calame, D. Poulidakos, M. V. Kovalenko, and I. Shorubalko, "Nanoprinted Quantum Dot–Graphene Photodetectors," *Advanced Optical Materials*, vol. 7, no. 11, 2019.

- [29] G. Kara, S. Bolat, K. Sharma, M. J. Grotevent, D. N. Dirin, D. Bachmann, R. Furrer, L. F. Boesel, Y. E. Romanyuk, R. M. Rossi, M. V. Kovalenko, M. Calame, and I. Shorubalko, "Conformal Integration of an Inkjet-Printed PbS QDs-Graphene IR Photodetector on a Polymer Optical Fiber," *Advanced Materials Technologies*, vol. 2201922, 2023.
- [30] F. H. Koppens, T. Mueller, P. Avouris, A. C. Ferrari, M. S. Vitiello, and M. Polini, "Photodetectors based on graphene, other two-dimensional materials and hybrid systems," *Nature Nanotechnology*, vol. 9, no. 10, pp. 780–793, 2014.
- [31] R. Saran and R. J. Curry, "Lead sulphide nanocrystal photodetector technologies," *Nature Photonics*, vol. 10, no. 2, pp. 81–92, 2016.
- [32] N. Huo and G. Konstantatos, "Recent progress and future prospects of 2D-based photodetectors," *Advanced Materials*, vol. 30, no. 51, 2018.
- [33] H. Fang and W. Hu, "Photogating in Low Dimensional Photodetectors," *Advanced Science*, vol. 4, no. 12, 2017.
- [34] B. E. A. Saleh and M. C. Teich, *Fundamentals of photonics*. Wiley series in pure and applied optics, Hoboken, New Jersey: Wiley, 2nd ed., 2007.
- [35] I. Moreels, K. Lambert, D. Smeets, D. De Muynck, T. Nollet, J. C. Martins, F. Vanhaecke, A. Vantomme, C. Delerue, G. Allan, and Z. Hens, "Size-dependent optical properties of colloidal PbS quantum dots," *ACS Nano*, vol. 3, no. 10, pp. 3023–3030, 2009.
- [36] P. Galliker, J. Schneider, H. Eghlidi, S. Kress, V. Sandoghdar, and D. Poulidakos, "Direct printing of nanostructures by electrostatic autofocussing of ink nanodroplets," *Nature Communications*, vol. 3, no. 1, 2012.
- [37] M. S. Onses, E. Sutanto, P. M. Ferreira, A. G. Alleyne, and J. A. Rogers, "Mechanisms, Capabilities, and Applications of High-Resolution Electrohydrodynamic Jet Printing," *Small*, vol. 11, no. 34, pp. 4237–4266, 2015.
- [38] J. M. Luther, M. Law, Q. Song, C. L. Perkins, M. C. Beard, and A. J. Nozik, "Structural, Optical, and Electrical Properties of Self-Assembled Films of PbSe Nanocrystals Treated with 1,2-Ethanedithiol," *ACS Nano*, vol. 2, pp. 271–280, feb 2008.
- [39] C. H. M. Chuang, P. R. Brown, V. Bulović, and M. G. Bawendi, "Improved performance and stability in quantum dot solar cells through band alignment engineering," *Nature Materials*, vol. 13, no. 8, pp. 796–801, 2014.
- [40] M. Albaladejo-Siguan, E. C. Baird, D. Becker-Koch, Y. Li, A. L. Rogach, and Y. Vaynzof, "Stability of Quantum Dot Solar Cells: A Matter of (Life)Time," *Advanced Energy Materials*, vol. 11, no. 12, 2021.
- [41] Z. Wu, Y. Ou, M. Cai, Y. Wang, R. Tang, and Y. Xia, "Short-Wave Infrared Photodetectors and Imaging Sensors Based on Lead Chalcogenide Colloidal Quantum Dots," *Advanced Optical Materials*, vol. 11, no. 1, 2023.
- [42] Y. Q. Huang, R. J. Zhu, N. Kang, J. Du, and H. Q. Xu, "Photoelectrical response of hybrid graphene-PbS quantum dot devices," *Applied Physics Letters*, vol. 103, no. 14, 2013.
- [43] X. Du, I. Skachko, A. Barker, and E. Y. Andrei, "Approaching ballistic transport in suspended graphene," *Nature Nanotechnology*, vol. 3, no. 8, pp. 491–495, 2008.
- [44] A. Dorodnyy, Y. Salamin, P. Ma, J. Vukajlovic Plestina, N. Lassaline, D. Mikulik, P. Romero-Gomez, A. Fontcuberta i Morral, and J. Leuthold, "Plasmonic Photodetectors," *IEEE Journal of Selected Topics in Quantum Electronics*, vol. 24, no. 6, 2018.
- [45] M. J. Grotevent, C. U. Hail, S. Yakunin, D. Bachmann, G. Kara, D. N. Dirin, M. Calame, D. Poulidakos, M. V. Kovalenko, and I. Shorubalko, "Temperature-Dependent Charge Carrier Transfer in Colloidal Quantum Dot/Graphene Infrared Photodetectors," *ACS Applied Materials & Interfaces*, vol. 13, pp. 848–856, jan 2021.
- [46] R. Wang, Y. T. Zhang, H. Y. Wang, X. X. Song, L. F. Jin, and J. Q. Yao, "Wide spectral response field-effect phototransistor based on graphene-quantum dot hybrid," *IEEE Photonics Journal*, vol. 7, no. 2, 2015.

-
- [47] A. A. Balandin, “Low-frequency $1/f$ noise in graphene devices,” *Nature Nanotechnology*, vol. 8, no. 8, pp. 549–555, 2013.
- [48] R. H. Bube, *Photoconductivity of solids*. New York: Wiley, 2nd ed., 1967.
- [49] G. Konstantatos and E. H. Sargent, “PbS colloidal quantum dot photoconductive photodetectors: Transport, traps, and gain,” *Applied Physics Letters*, vol. 91, no. 17, p. 173505, 2007.
- [50] F. Xia, T. Mueller, R. Golizadeh-Mojarad, M. Freitag, Y. M. Lin, J. Tsang, V. Perebeinos, and P. Avouris, “Photocurrent imaging and efficient photon detection in a graphene transistor,” *Nano Letters*, vol. 9, no. 3, pp. 1039–1044, 2009.
- [51] P. Karnatak, T. Paul, S. Islam, and A. Ghosh, “ $1/f$ noise in van der Waals materials and hybrids,” *Advances in Physics: X*, vol. 2, no. 2, pp. 428–449, 2017.
- [52] E. Simoen and C. Claeys, “On the flicker noise in submicron silicon MOSFETs,” *Solid-State Electronics*, vol. 43, no. 5, pp. 865–882, 1999.
- [53] Z. Wu, S. Wu, S. Oberholzer, M. Steinacher, M. Calame, and C. Schönenberger, “Scaling of $1/f$ noise in tunable break junctions,” *Physical Review B*, vol. 78, no. 23, 2008.
- [54] S. Rumyantsev, G. Liu, W. Stillman, M. Shur, and A. A. Balandin, “Electrical and noise characteristics of graphene field-effect transistors: Ambient effects, noise sources and physical mechanisms,” *Journal of Physics Condensed Matter*, vol. 22, no. 39, 2010.
- [55] I. Heller, S. Chatoor, J. Männik, M. A. Zevenbergen, J. B. Oostinga, A. F. Morpurgo, C. Dekker, and S. G. Lemay, “Charge noise in graphene transistors,” *Nano Letters*, vol. 10, no. 5, pp. 1563–1567, 2010.
- [56] P. Karnatak, T. P. Sai, S. Goswami, S. Ghatak, S. Kaushal, and A. Ghosh, “Current crowding mediated large contact noise in graphene field-effect transistors,” *Nature Communications*, vol. 7, no. 1, 2016.
- [57] M. A. Hines and G. D. Scholes, “Colloidal PbS Nanocrystals with Size-Tunable Near-Infrared Emission: Observation of Post-Synthesis Self-Narrowing of the Particle Size Distribution,” *Advanced Materials*, vol. 15, no. 21, pp. 1844–1849, 2003.
- [58] F. V. Antolinez, J. M. Winkler, P. Rohner, S. J. P. Kress, R. C. Keitel, D. K. Kim, P. Marqués-Gallego, J. Cui, F. T. Rabouw, D. Poulidakos, and D. J. Norris, “Defect-Tolerant Plasmonic Elliptical Resonators for Long-Range Energy Transfer,” *ACS Nano*, vol. 13, pp. 9048–9056, aug 2019.